Research Square

Preprints are preliminary reports that have not undergone peer review.
They should not be considered conclusive, used to inform clinical practice,
or referenced by the media as validated information.

Synergistic thermal conduction and electromagnetic shielding in nickel foam-based composite via boron nitride and high- entropy oxide@Ag

Qi Zeng
Shanghai University of Engineering Science
Binkai Hu
Shanghai University of Engineering Science
Shihua Yang
Shanghai Aerospace Equipments Manufacturer Co., Ltd.
Shengyu Wu
Shanghai RedEDA Co., Ltd.
Xinlei Wang
Shanghai University of Engineering Science
Bin Li
libin@sues.edu.cn
Shanghai University of Engineering Science
An-Quan Xie
Shanghai University of Engineering Science
Chunjin Hang
Harbin Institute of Technology

Research Article

Keywords: Thermal conductivity, Electromagnetic shielding, Nickel foam, BN nanosheets, High-entropy oxide

Posted Date: July 23rd, 2026

DOI: https://doi.org/10.21203/rs.3.rs-10413997/v1

License: This work is licensed under a Creative Commons Attribution 4.0 International License.
Read Full License

Additional Declarations: No competing interests reported.

Abstract

A multifunctional composite was strategically designed to simultaneously address thermal management and electromagnetic interference (EMI) shielding challenges in next-generation high-performance electronics. The composite was fabricated by filling a three-dimensional nickel foam with a waterborne polyurethane (WPU) matrix containing BN nanosheets and core–shell $(FeCoNiMgMn)_3O_4$@Ag fillers. Microstructural characterization confirmed uniform dispersion of BN nanosheets and successful Ag immobilization onto the high-entropy oxide surface. The optimized Ni/WPU-BN composite achieved a thermal conductivity of 0.91 W/m·K, nearly threefold enhancement over pristine WPU. It was found that the high-entropy oxide could improve impedance matching, facilitating greater electromagnetic wave penetration into the material for dissipative absorption. Concurrently, the Ni/WPU-BN-$(FeCoNiMgMn)_3O_4$@Ag composite exhibited an excellent EMI shielding effectiveness of 67.2 dB with absorption as the dominant mechanism. And finite element simulations further validated the experimental shielding trends. This work presents a promising dual-network strategy for advanced electronic packaging materials with integrated thermal and electromagnetic functionalities.

1. Introduction

As electronic devices continue to evolve toward miniaturization, high integration, and high-power density, thermal failure and electromagnetic pollution have become increasingly prominent, posing critical bottlenecks to the reliability and lifetime of next-generation high-performance electronic systems. Progressive heat buildup within devices accelerates material degradation, compromises operational efficiency, and may even induce catastrophic thermal runaway. Concurrently, electromagnetic interference (EMI) induces signal distortion and data corruption, and can trigger cross-device interference, thereby undermining communication quality and system stability. Therefore, the development of multifunctional materials that simultaneously integrate superior thermal management and efficient EMI shielding capabilities holds significant promise for ensuring the reliable operation of modern electronic systems.

In recent years, micro/nanomaterials have shown great promise for applications in thermal management [1, 2], EMI shielding [3, 4], sensing [5], energy harvesting [6], disease detection [7], and flexible electronics [8]. Among these, nickel foam has garnered considerable attention for EMI shielding applications due to its unique three-dimensional porous network, good electrical conductivity, excellent magnetic loss properties, and high mechanical strength [9]. Although nickel foam demonstrates strong microwave absorption, its thermal conductivity remains significantly inferior to that of high thermal conductivity metals such as copper foam, making it insufficient for the heat dissipation requirements of high-density integrated electronic packaging. Moreover, the EMI shielding of pure nickel foam relies primarily on reflection loss, whereby incident electromagnetic waves are largely reflected at the material surface. Although this yields high EMI shielding effectiveness (EMI SE), the reflected waves may cause secondary EMI in surrounding sensitive components.

Boron nitride nanosheets, graphene-like two-dimensional materials, exhibit ultrahigh thermal conductivity, excellent electrical insulation, and outstanding chemical stability, making them ideal fillers for constructing three-dimensional thermally conductive networks [10]. The unique high-entropy effect, lattice distortion effect, sluggish diffusion effect, and cocktail effect of high-entropy oxides confer properties unavailable in conventional single-component oxides. In particular, spinel-structured high-entropy ferrites can induce rich magnetic dipole interactions and dielectric polarization, thereby achieving excellent impedance matching between dielectric and magnetic losses for electromagnetic wave absorption [11]. However, single-phase high-entropy oxides generally suffer from low electrical conductivity, which limits their contribution to reflection loss in EMI shielding applications. Silver, the most electrically conductive metal, offers superior EMI SE through strong reflection [12]. Coating high-entropy spinel oxides with silver layers yields a core–shell ferrite@Ag architecture that couples the magnetic/dielectric losses of oxide phase with the high electrical conductivity of silver.

This study aims to achieve a synergistic enhancement of the thermal conductivity and EMI shielding performance of nickel foam while preserving its inherent microwave absorption advantages. Using three-dimensional nickel foam as the scaffold, highly thermally conductive BN nanosheets were first incorporated to overcome the inherently low thermal conductivity of the foam. Subsequently, high-entropy ferrite@Ag composite fillers with excellent EMI shielding properties were introduced to synergistically improve the EMI SE. In addition, the micro-morphology, crystal structure, and surface chemistry of the samples were systematically characterized, and the thermal conductivity and EMI SE were evaluated.

2. Experimental

Initially, 0.5 g of BN powder and 15 g of urea were ball-milled at 400 r/min for 10 h. Then, deionized water was added, and the mixture was ball-milled for an additional 1 h to ensure complete dissolution of urea. The product was washed three times with deionized water and ethanol, centrifuged at 10000 r/min after each wash, and finally dried at 80°C to yield exfoliated BN nanosheets. The BN powder used in this study was purchased from Shanghai Yansu Technology Co., Ltd. (Shanghai, China; mall.shiyanjia.com).

Subsequently, $FeCl_3{\cdot}6H_2O$, $CoCl_2{\cdot}6H_2O$, $NiCl_2{\cdot}6H_2O$, $MgCl_2{\cdot}6H_2O$, and $Mn(NO_3)_2{\cdot}xH_2O$ (1.5 mmol each) were dissolved in 40 mL of ethylene glycol and magnetically stirred at room temperature for 10 min to obtain a homogeneous solution. Next, 3.6 g of sodium acetate and 1.0 g (0.888 mL) of polyethylene glycol 400 were added, and the mixture was stirred for an additional 20 min. The resulting mixture was then transferred into a 100 mL Teflon-lined stainless-steel autoclave and heated at 200°C for 20 h. After cooling to room temperature, the product was collected by centrifugation at 10000 r/min, and then washed three times sequentially with deionized water and ethanol. The product was then dried at 80°C and ground into powder to yield $(FeCoNiMgMn)_3O_4$ nanomaterials.

Then, 0.061 g of tris(hydroxymethyl)aminomethane hydrochloride (Tris) was dissolved in 50 mL of deionized water under magnetic stirring to obtain a Tris buffer solution (pH 8.5). Subsequently, 0.1 g of

dopamine hydrochloride (DA) was added to the above solution and magnetically stirred to yield a 2 mg/mL DA solution. 0.2 g of the as-ground $(FeCoNiMgMn)_3O_4$ was then dispersed in the DA solution, sonicated for 10 min, and subsequently subjected to slow magnetic stirring for 12 h. The resultant precipitate was collected by centrifugation at 10000 r/min, washed alternately with deionized water and ethanol three times, and dried at 60°C for 1 h to prepare the $(FeCoNiMgMn)_3O_4$@polydopamine (PDA). Separately, 0.3 g of $AgNO_3$ was dissolved in 15 mL of deionized water under magnetic stirring to prepare a 20 mg/mL $AgNO_3$ solution. The as-obtained $(FeCoNiMgMn)_3O_4$@PDA powder was then immersed in this solution for 30 min. Meanwhile, 4.5 g of glucose and 1.5 g of potassium sodium tartrate tetrahydrate were dissolved in 15 mL of deionized water under magnetic stirring. This reducing mixture was then added dropwise to the $AgNO_3$ solution containing the pre-immersed $(FeCoNiMgMn)_3O_4$@PDA. After magnetic stirring at room temperature for 3 h, the product was collected by centrifugation at 10000 r/min, washed alternately with deionized water and ethanol three times, and dried at 60°C to obtain $(FeCoNiMgMn)_3O_4$@Ag.

Finally, a 0.5 mm thick nickel foam was ultrasonicated in 5 M HCl solution for 20 min to remove the surface NiO layer, followed by rinsing with deionized water and ethanol several times. Subsequently, 1.02 g of waterborne polyurethane (WPU, 40% solid content) was placed in a centrifuge tube, followed by adding 0.117 g of ball-milled BN nanosheets. After ultrasonication for 20 min, 0.058 g of $(FeCoNiMgMn)_3O_4$@Ag was added, and the mixture was further ultrasonicated for 20 min to yield a uniform suspension. The suspension was blade-coated onto the Ni foam and allowed to penetrate into the pores, the resulting sample was then dried at 60°C for 12 h to obtain the final Ni/WPU-BN-$(FeCoNiMgMn)_3O_4$@Ag composite.

The general morphology and elemental distribution were investigated using scanning electron microscopy (SEM, ZEISS GeminiSEM 300) coupled with energy dispersive spectroscopy (EDS). An FEI Talos F200X instrument was employed for transmission electron microscopy (TEM) analysis. A vector network analyzer (Agilent E5071C) was utilized to measure the reflection loss and EMI SE. X-ray diffraction (XRD) was conducted on a Rigaku SmartLab SE diffractometer to characterize the phase composition. Measurements of the thermal conductivity were performed by a thermal constants analyzer (Hot Disk TPS 2500S). The surface chemical states were carried out via X-ray photoelectron spectroscopy (XPS, PHI 5000 VersaProbe). ANSYS High-Frequency Structure Simulator (HFSS) served as the platform for finite element simulations.

3. Results and discussion

The SEM images of nickel foam at different magnifications (Fig. 1a and b) reveal a characteristic three-dimensional interconnected architecture with uniformly distributed pores. The continuous metallic scaffold constitutes a long-range ordered network, which provides ample void space for the infiltration of WPU matrix and the accommodation of functional fillers. As shown in the SEM image (Fig. 1c), the ball-milled BN nanosheets display a characteristic two-dimensional lamellar morphology with an overall near-

circular shape. Although mild agglomeration is observed among the nanosheets, individual lamellae remain clearly distinguishable. This two-dimensional structure allows the BN nanosheets to overlap within the polymer matrix, thereby establishing continuous thermal conductive pathways and reducing the intrinsic thermal resistance of the WPU matrix. Moreover, the large specific surface area of BN nanosheets offers abundant anchoring sites for further loading of high-entropy ferrite@Ag nanomaterials, which is conducive to the development of multi-component heterogeneous interfaces. TEM imaging (Fig. 1d) confirms the nanometer-scale thickness of the ball-milled BN nanosheets. This ultrathin lamellar architecture minimizes interlayer phonon–phonon scattering, enabling efficient in-plane phonon transport and thus improved thermal conductivity in the composites.

Figure 2 displays three-dimensional reflection loss figures and corresponding two-dimensional contour maps of ball-milled nickel foam powders mixed with paraffin, covering the frequency range of 2–18 GHz and thickness range of 0–8 mm, to reveal the effect of conductive filler content on electromagnetic wave attenuation. At a filler/matrix mass ratio of 3:7 (Fig. 2a and b), the Ni/paraffin composite exhibits poor electromagnetic wave attenuation, with reflection loss values remaining above − 10 dB. This observation is in accordance with the previous report for high entropy spinel ferrite [13], where effective absorption was not achieved at filler mass fractions below 30%. This can be ascribed to the insufficient intrinsic loss ability of the material at low filler contents, which is inadequate for dissipating the energy of incident electromagnetic waves. As the Ni/paraffin ratio increases to 7:3, the composite presents significantly improved microwave absorption (Fig. 2c and d). A minimum reflection loss of − 56.4 dB is achieved, along with a remarkably broadened effective absorption bandwidth. Notably, rather than causing severe impedance mismatch, this high filler loading leads to a substantial enhancement in microwave absorption performance.

As shown in Fig. 3a, the pristine WPU sample exhibits a broad diffraction peak centered at 20°, which is characteristic of an amorphous structure with no detectable crystalline phase. The Ni/WPU composite shows three characteristic diffraction peaks at 44.5°, 51.8°, and 76.4° alongside the retained broad amorphous peak of WPU. These peaks are assigned to the (111), (200), and (220) planes of face-centered cubic Ni, respectively [14]. This result confirms the structural stability of nickel foam during composite fabrication, thus retaining its intrinsic high electrical and thermal conductivity. With the further addition of BN nanosheets, the Ni/WPU-BN composite displays diffraction peaks at 26.7°, 41.6°, and 54.9°, which are indexed as the (002), (100), and (004) planes of hexagonal BN [15], while retaining the amorphous peak of WPU and characteristic peaks of Ni. This verifies the successful incorporation of BN nanosheets into the composite with an intact crystalline structure. Figure 3b presents a comparison of room-temperature thermal conductivities for three samples. The pristine WPU matrix exhibits a thermal conductivity of 0.31 W/m·K, which is characteristic of insulating polymers. With the introduction of three-dimensional continuous nickel foam scaffold, the thermal conductivity of Ni/WPU composite increases substantially compared to that of WPU. This improvement is attributed to the formation of continuous thermal conductive pathways, confirming the reinforcing role of nickel foam in thermal conduction. Furthermore, the thermal conductivity of Ni/WPU-BN composite increases further to 0.91 W/m·K due to the synergistic effect of a hierarchical thermal conductive network. The two-dimensional

BN nanosheets are uniformly dispersed within the WPU matrix and interconnected, thereby forming a microscale thermal conductive network.

Figure 4a presents a low-magnification cross-sectional SEM image of the Ni/WPU-BN composite, revealing a tightly interlocked interfacial structure between the three-dimensional nickel foam and WPU-BN filler. The interface appears flat and continuous, indicating favorable wettability of the nickel foam surface by WPU. The Ni elemental mapping in Fig. 4b is in excellent agreement with the nickel scaffold morphology observed in Figure 4a. The N elemental mapping in Fig. 4c exhibits a uniform distribution of nitrogen throughout the WPU-BN filler. This nitrogen originates from both the BN nanosheets and WPU matrix, suggesting homogeneous dispersion of the BN nanosheets without obvious agglomeration. The coexistence of Ni and N characteristic peaks in EDS spectrum (Fig. 4f) further confirm the successful preparation of the Ni/WPU-BN composite. Figure 4d and e show SEM images of the WPU-BN filler region within the same cross-section at different magnifications. The BN nanosheets are observed to be uniformly dispersed within the WPU matrix without visible defects such as voids.

Figure 5a and b show SEM images of the $(FeCoNiMgMn)_3O_4$ nanostructure at different magnifications. The high-entropy oxide is composed of nanoflowers and nanoparticles with good overall dispersion. The nanoflowers consist of numerous ultrathin wrinkled nanosheets stacked together, yielding a typical hierarchically porous structure. Such a hierarchical architecture not only provides abundant surface-active sites and phase interfaces, but also enables multiple internal reflection and scattering of incident electromagnetic waves, thus extending the propagation path and facilitating enhanced electromagnetic loss. Figure 5c and d present SEM images of the $(FeCoNiMgMn)_3O_4$@Ag composite. The Ag-coated sample maintains a particle size distribution and overall dispersion comparable to the as-synthesized high-entropy oxide. Furthermore, the $(FeCoNiMgMn)_3O_4$@Ag consists solely of quasi-spherical nanoparticles, suggesting that the original nanoflowers assembled from wrinkled nanosheets have been coated with Ag.

The phase compositions of $(FeCoNiMgMn)_3O_4$ and $(FeCoNiMgMn)_3O_4$@Ag are displayed in Fig. 6a. For the $(FeCoNiMgMn)_3O_4$ sample, characteristic diffraction peaks are observed at 30.2°, 35.6°, 43.3°, and 62.8°, assigned to the (220), (311), (400), and (440) planes of spinel structure, respectively [16]. No diffraction peaks from impurity phases are detected, confirming the successful synthesis of the spinel-structured high-entropy oxide. After Ag coating, the $(FeCoNiMgMn)_3O_4$@Ag sample retains the characteristic peaks of as-synthesized high-entropy oxide, while three additional sharp peaks appear at 38.1°, 64.4°, and 77.5°, indexed to the (111), (220), and (311) planes of Ag, respectively. These findings verify the successful immobilization of Ag on the high-entropy oxide surface. Subsequently, XPS was performed to further elucidate the surface elemental composition and chemical states of $(FeCoNiMgMn)_3O_4$@Ag composite. In the Fe 2p spectrum (Fig. 6b), peaks at 711.2 and 723.8 eV are attributed to Fe^{3+}, while peaks at 709.6 and 720.1 eV are assigned to Fe^{2+}. The high-resolution Co 2p spectrum in Fig. 6c also shows mixed-valence characteristics of Co^{2+} and Co^{3+}. In the high-resolution Ni 2p spectrum, peaks at 855.7 and 873.2 eV are ascribed to Ni^{2+} (Fig. 6d). The Mg 1s spectrum in Fig. 6e

exhibits a single peak at 1303.8 eV corresponding to Mg^{2+} within the spinel lattice, confirming the successful incorporation of Mg. The high-resolution Mn 2p spectrum can be resolved into two valence-state components corresponding to Mn^{2+} and Mn^{3+} (Fig. 6f). The characteristic peaks located at 644.1 and 655.7 eV are assigned to Mn^{2+}, while those at 639.6 and 651.4 eV are attributed to Mn^{3+}. As shown in Fig. 6g, the O 1s spectrum displays a strong characteristic peak centered at 531.5 eV. The Ag 3d spectrum in Fig. 6h shows a spin–orbit doublet at 368.2 eV (Ag $3d_{5/2}$) and 374.2 eV (Ag $3d_{3/2}$), which are in agreement with the binding energies for metallic Ag. This confirms that the loaded Ag exists in its metallic state without detectable oxidation. For the C 1s spectrum (Fig. 6i), the binding energy scale was referenced to the adventitious C–C component at 284.8 eV.

Figure 7a illustrates a quantitative comparison of the total SE (SE_T), reflection SE (SE_R), and absorption SE (SE_A) for three samples. When the material thickness exceeds the skin depth, SE_T can be approximated by the sum of SE_R and SE_A. The results demonstrate that SE_T is progressively enhanced with the sequential introduction of $(FeCoNiMgMn)_3O_4$ and $(FeCoNiMgMn)_3O_4$@Ag fillers. For the Ni/WPU-BN system, the three-dimensional continuous nickel foam constructs a macroscopic conductive network that endows the composite with inherent shielding capability. The SE_T of this sample reaches 50.3 dB with SE_R exceeding SE_A, indicating that reflection dominates the shielding process. With the addition of $(FeCoNiMgMn)_3O_4$, the composite achieves a SE_T of 56.2 dB with the improvement mainly originating from increased SE_A. The high-entropy oxide also improves impedance matching, facilitating greater electromagnetic wave penetration into the material for dissipative absorption. Consequently, the SE_R decreases marginally, while the SE_T rises due to the dominant absorption contribution. Following the incorporation of $(FeCoNiMgMn)_3O_4$@Ag filler, the SE_T of composite increases further to 67.2 dB. Notably, both SE_R and SE_A increase simultaneously with SE_A becoming the dominant contribution. In order to intuitively reveal the propagation and attenuation characteristics of electromagnetic waves inside the composites, a rectangular waveguide simulation model was constructed, as shown in Fig. 7b–g. It can be seen that the Ni/WPU-BN sample exhibits weak electromagnetic attenuation (Fig. 7b and e). With the introduction of $(FeCoNiMgMn)_3O_4$, the field intensity decreases significantly as the waves propagate through the material (Fig. 7c and f). For the composite incorporating $(FeCoNiMgMn)_3O_4$@Ag filler, the attenuation is most pronounced (Fig. 7d and g). Overall, the simulated field attenuation is in excellent agreement with the experimental shielding trend.

4. Conclusions

In summary, a multifunctional Ni/WPU-BN-$(FeCoNiMgMn)_3O_4$@Ag composite was successfully fabricated by integrating a three-dimensional nickel foam with thermally conductive BN nanosheets and core–shell high-entropy ferrite@Ag fillers. The morphology and phase structure of as-prepared samples could be directly detected from SEM, TEM, XRD and XPS characterization. We found that BN nanosheets exhibited uniform dispersion within the WPU matrix and favorable interfacial compatibility with the nickel foam. In addition, the thermal conductivity and EMI SE of the composites were systematically evaluated.

It was found that the hierarchical thermal conductive network and multiple electromagnetic loss mechanisms could distinctly improve the overall performance of the composites. In particular, the optimized composite achieved a thermal conductivity of 0.91 W/m·K and an excellent EMI SE of 67.2 dB. Moreover, the EMI shielding performance was investigated through both experimental measurements and finite element simulations.

Declarations

Conflict of interest

The authors declare that they have no known competing financial interests or personal relationships that could have appeared to influence the work reported in this paper.

Funding

This work was supported by State Key Laboratory of Precision Welding & Joining of Materials and Structures (No. MSWJ-26M-22).

Author Contribution

Qi Zeng, Bin Li, An-Quan Xie, and Chunjin Hang contributed to the study design and writing. The material preparation, data collection, and data analysis were performed by Qi Zeng, Binkai Hu, Shihua Yang, Shengyu Wu, and Xinlei Wang.

Acknowledgement

This work was supported by State Key Laboratory of Precision Welding & Joining of Materials and Structures (No. MSWJ-26M-22).

Data availability

All data generated or analyzed during this study are included in this article.

References

1. M. He, X. Zhong, X. Lu, J. Hu, K. Ruan, H. Guo, Y. Zhang, Y. Guo, J. Gu, Adv. Mater. **36**, 2410186 (2024)
2. K. Zhao, S. Wei, M. Cao, M. Wang, P. Li, H. Li, X. Zhang, Y. Zhang, Y. Chen, Compos. Sci. Technol. **245**, 110323 (2024)

3. N. Harshini, I.D. Bhavani, N. Dileep, C.A. Babu, S.A.V. Prasad, C. Srinivas, C.R.S. Hanuman, M. Ismail, E.R. Kumar, S.K. Rout, S.S. Meena, Ceram. Int. **51**, 17246 (2025)
4. Y. Zhang, K. Ruan, K. Zhou, J. Gu, Adv. Mater. **35**, 2211642 (2023)
5. H. Liu, B. Li, J. Guo, M. Zhang, N. Lu, Sens. Actuators B Chem. **457**, 139697 (2026)
6. G. Shan, S. Chen, H. Li, Y. Jia, G. Wang, H. Sun, Y. Guo, Adv. Funct. Mater. e76493 (2026)
7. Y. Xiao, M. Zhang, N. Lu, Anal. Chem. **97**, 4978 (2025)
8. X. Wang, F. Liu, Y. Guo, H. Zhang, Y. Li, Q. Xi, X. Han, W. Gong, Small **22**, e12821 (2026)
9. Y. Zhang, R. Liu, C. Liu, Y. Zhang, L. Yan, J. Jiang, E. Liu, F. Xu, J. Mater. Sci. Technol. **215**, 258 (2025)
10. G. Han, H. Cheng, C. He, Y. Feng, C. Liu, Compos. Commun. **34**, 101267 (2022)
11. J. Ma, B. Zhao, H. Xiang, F.Z. Dai, Y. Liu, R. Zhang, Y. Zhou, J. Adv. Ceram. **11**, 754 (2022)
12. Y. Bai, B. Zhang, J. Ma, Y. Cheng, P. Cui, Y. Kang, F. Wu, C. Chen, W. Huang, Small. **21**, 2408950 (2025)
13. F.H. Mohammadabadi, S.M. Masoudpanah, S. Alamolhoda, H.R. Koohdar, J. Mater. Res. Technol. **14**, 1099 (2021)
14. H. Li, X. Gao, G. Li, Small. **19**, 2304081 (2023)
15. X. Wang, X. Wang, S. Yang, M. Zhu, B. Hu, K. Liu, H. Liu, B. Li, J. Mater. Sci. -Mater Electron. **37**, 810 (2026)
16. B. Li, H. Liu, X. Xing, C. Zeng, M. Zhang, H. Li, N. Lu, ACS Appl. Nano Mater. **7**, 20985 (2024)

Figures

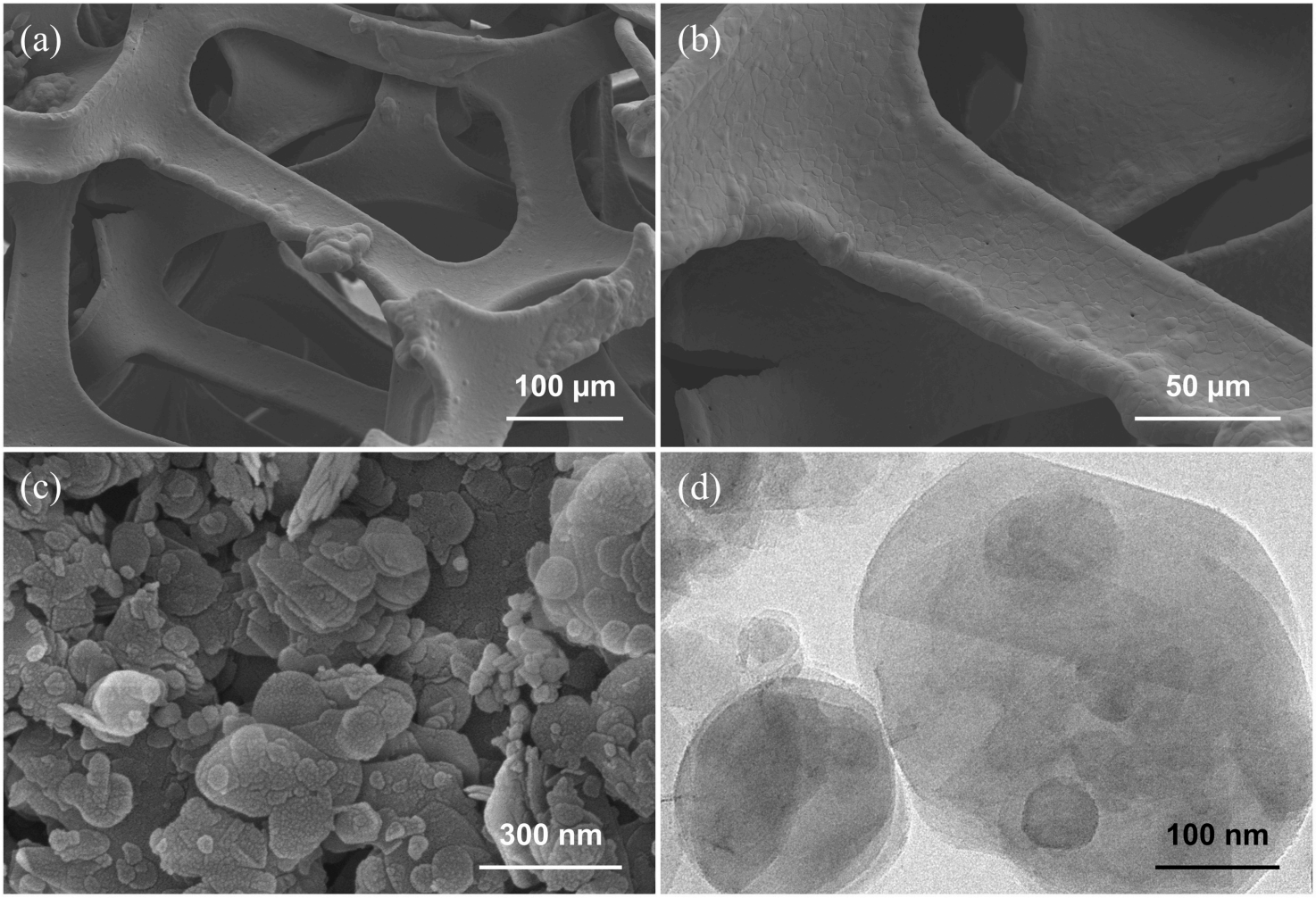


Figure 1

SEM images of **a, b** nickel foam, **c** SEM image and **d** TEM image of BN nanosheets

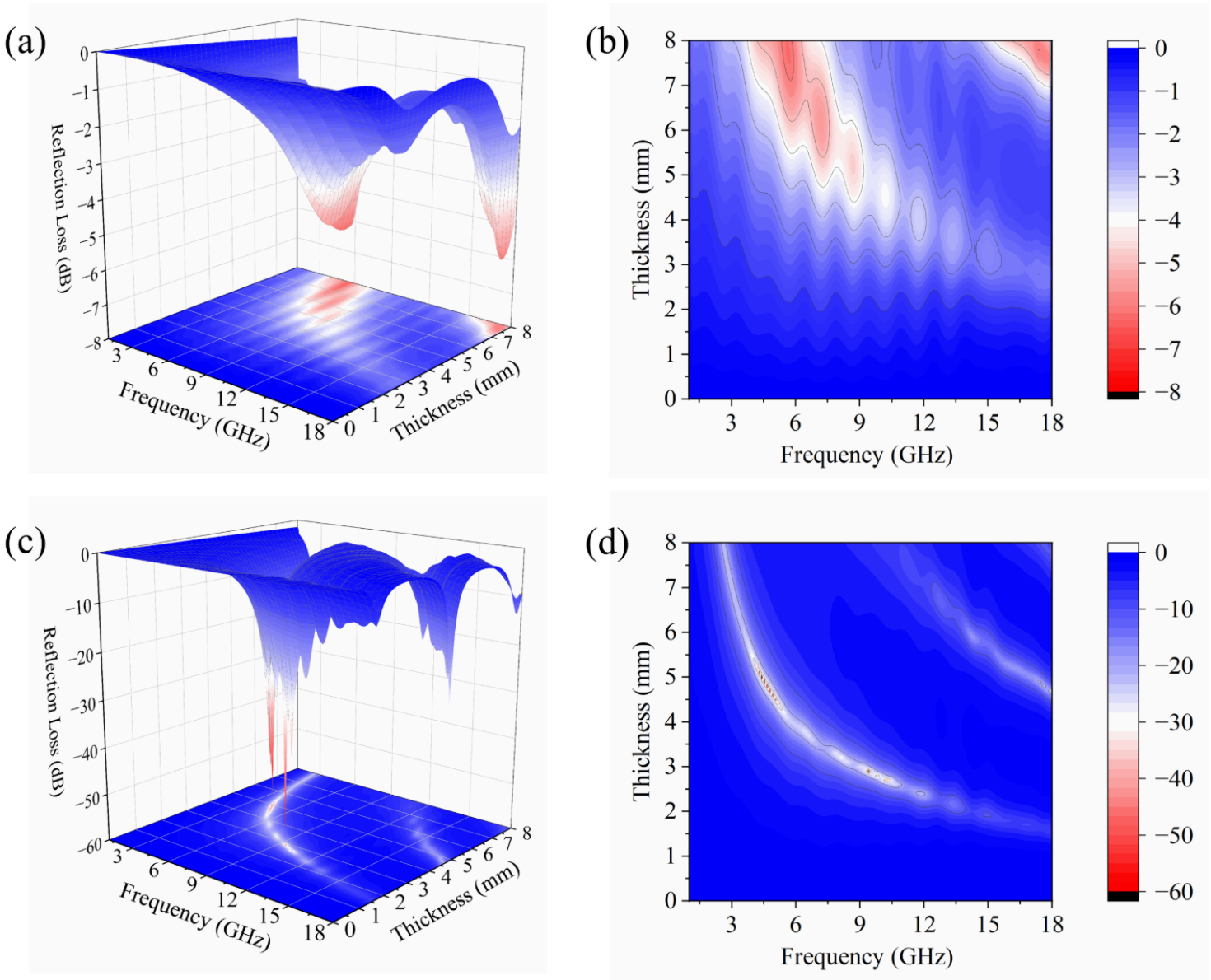


Figure 2

Three-dimensional reflection loss figures and two-dimensional reflection loss contour maps of ball-milled nickel foam powders mixed with paraffin at the mass ratio of **a, b** 3:7 and **c, d** 7:3

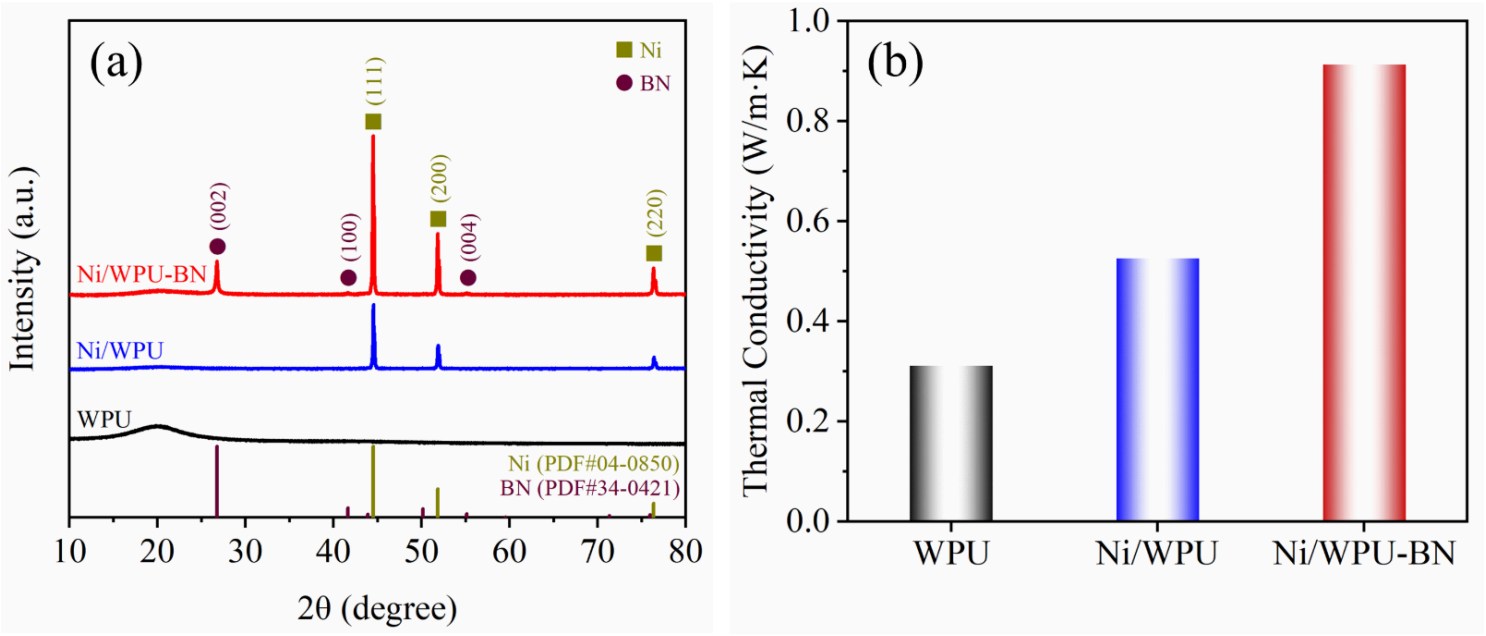


Figure 3

a XRD patterns and **b** thermal conductivities of WPU, Ni/WPU, and Ni/WPU-BN samples

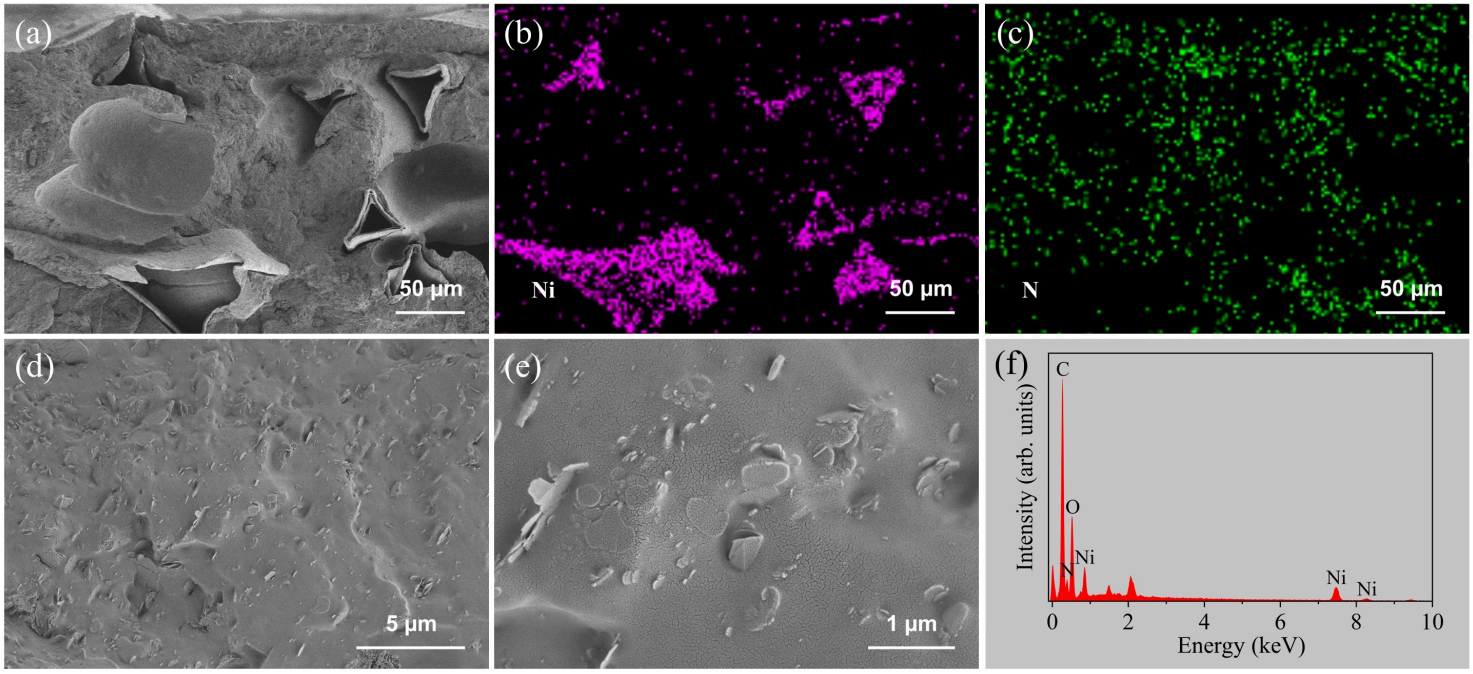


Figure 4

a–c Element distribution maps and **f** EDS spectrum of Ni/WPU-BN composite cross-section, **d, e** SEM images of the WPU-BN region in the same cross-section

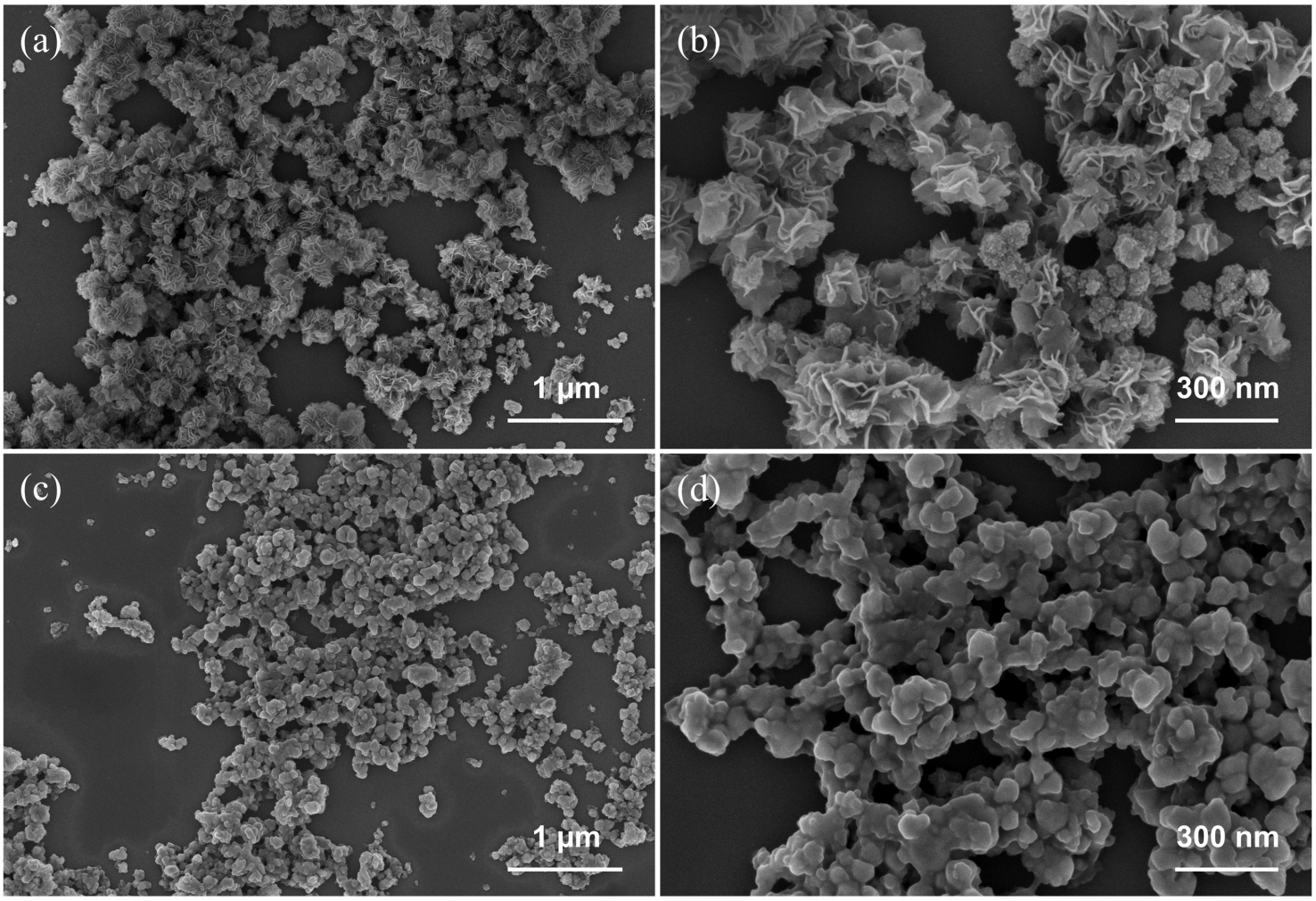


Figure 5

SEM images of **a, b** $(FeCoNiMgMn)_3O_4$ and **c, d** $(FeCoNiMgMn)_3O_4$@Ag

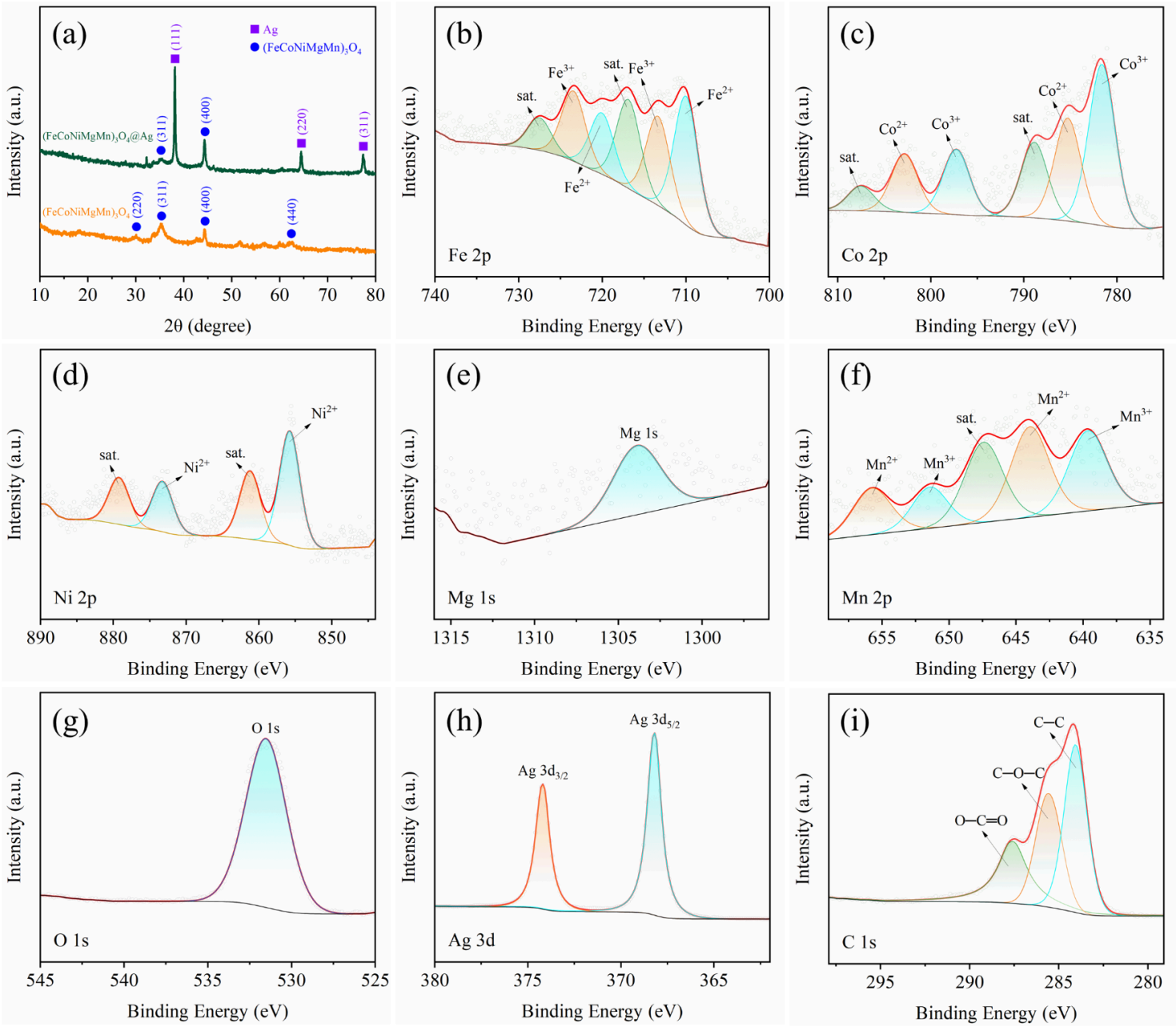


Figure 6

a XRD patterns of $(FeCoNiMgMn)_3O_4$ and $(FeCoNiMgMn)_3O_4$@Ag, **b–i** XPS spectra of $(FeCoNiMgMn)_3O_4$@Ag

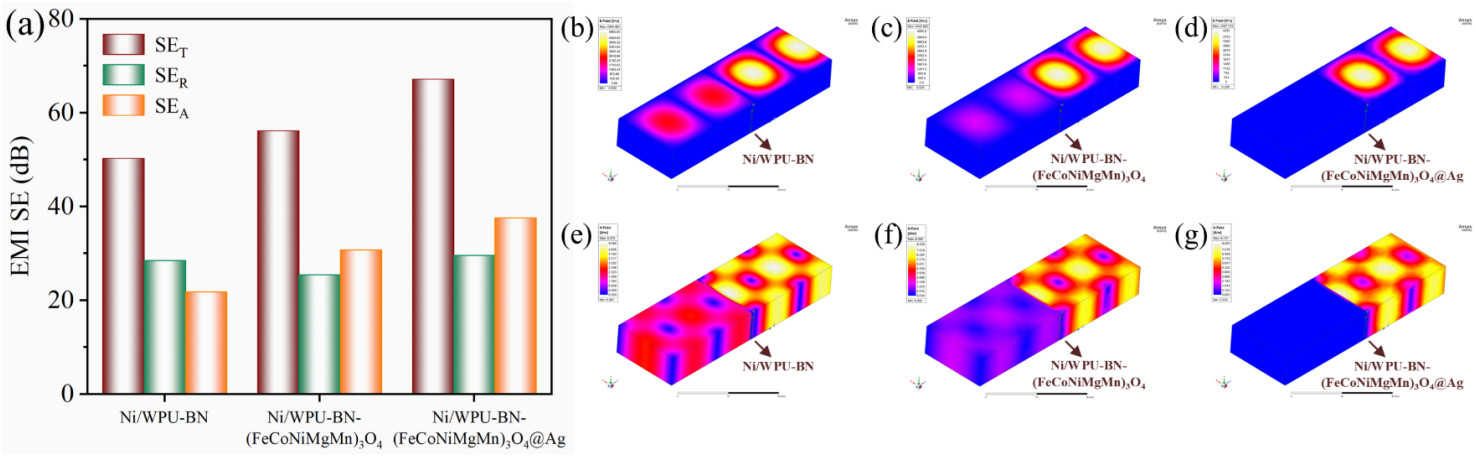


Figure 7

a EMI SE of Ni/WPU-BN, Ni/WPU-BN-$(FeCoNiMgMn)_3O_4$, and Ni/WPU-BN-$(FeCoNiMgMn)_3O_4$@Ag at 8.2 GHz, **b–d** simulated electric field distribution and **e–g** simulated magnetic field distribution of three samples (scale bar: 30 mm).